Journal of *Marine Science and Engineering*

MDPI

Article

Snow and Sea Ice Melt Enhance Under-Ice pCO_2 Undersaturation in Arctic Waters

Josefa Verdugo [1,*], Eugenio Ruiz-Castillo [1], Søren Rysgaard [1,2], Wieter Boone [3], Tim Papakyriakou [2], Nicolas-Xavier Geilfus [4] and Lise Lotte Sørensen [5]

[1] Department of Biology, Center for Ice-Free Arctic Research (CIFAR), Aarhus University, 8000 Aarhus, Denmark; eruizcas@bio.au.dk (E.R.-C.); rysgaard@bio.au.dk (S.R.)
[2] Centre for Earth Observation Science and Department of Environment and Geography, University of Manitoba, Winnipeg, MB R2C 0A1, Canada; tim.papakyriakou@umanitoba.ca
[3] Flanders Marine Institute (VLIZ), 8400 Oostende, Belgium; wieter.boone@vliz.be
[4] Tvärminne Zoological Station, University of Helsinki, 10901 Hanko, Finland; nicolas-xavier.geilfus@helsinki.fi
[5] Department of Environmental Science, Aarhus University, 4000 Roskilde, Denmark; lls@envs.au.dk
* Correspondence: josefa.verdugo@bio.au.dk

Abstract

The decline in Arctic summer sea ice alters air–sea gas exchange. Because the Arctic Ocean accounts for 5%–14% of global oceanic carbon uptake, understanding how sea ice melt impacts the ocean's carbon sink capacity is central to constraining future fluxes. In this study, we focus on Young Sound-Tyrolerfjord in Northeast Greenland to examine the sea ice−ocean interaction during the transition from melt onset to melt pond drainage. High-frequency measurements of partial pressure of CO_2 (pCO_2) and seawater physical properties were taken 2.5 m below the sea ice. Our results reveal that pCO_2 in the seawater was undersaturated (248–354 µatm) compared to the atmosphere (401 µatm), showing that the seawater has the potential to take up atmospheric CO_2 as the sea ice breaks up. The pCO_2 undersaturation was attributed to dilution resulting from mixing meltwater from snow and sea ice with the under-ice seawater. Additionally, the drainage of melt pond water that had been in contact with the atmosphere into the under-ice seawater further lowered pCO_2. Melt pond drainage represents an initial connection between the atmosphere and under-ice seawater through meter-thick sea ice during the summer thaw. Our study demonstrates that snow and sea ice melt reduce pCO_2 in under-ice seawater, enhancing its potential for atmospheric CO_2 uptake during sea ice breakup.

Keywords: under-ice pCO_2; high-frequency pCO_2 measurements; snow and sea ice meltwater; Arctic

Academic Editor: Anatoly Gusev

Received: 10 October 2025
Revised: 22 November 2025
Accepted: 24 November 2025
Published: 27 November 2025

Citation: Verdugo, J.; Ruiz-Castillo, E.; Rysgaard, S.; Boone, W.; Papakyriakou, T.; Geilfus, N.-X.; Sørensen, L.L. Snow and Sea Ice Melt Enhance Under-Ice pCO_2 Undersaturation in Arctic Waters. *J. Mar. Sci. Eng.* **2025**, *13*, 2257. https://doi.org/10.3390/jmse13122257

1. Introduction

Rapid Arctic warming has led to changes in summer sea ice extent, thickness, and volume [1–6]. Since 1979, summer sea ice extent has declined by ~45% [7]. In September 2022, the average monthly extent was 4.87 million km^2, among the lowest in the 44-year satellite record [8]. The ice cover is now dominated by first-year ice, which is thinner and more vulnerable to oceanic and atmospheric forcing than multi-year ice [9–11]. Because sea ice limits atmosphere-ocean gas exchange [12], reduced sea ice extent can alter the pathways of CO_2 in Arctic waters. The Arctic carbon cycle is complex, as multiple interacting processes can either increase or decrease CO_2 concentrations in surface seawater, thereby influencing air–sea CO_2 exchange. For instance, it was recently shown that progressive

loss of sea ice resulted in a CO_2 increase in the Arctic Ocean, through enhanced sea-air gas exchange and increasing sea surface temperature [13]. In contrast, thinner ice permits more light penetration into the underlying seawater [14,15], stimulating under-ice primary production and the associated drawdown of CO_2, e.g., [16]. During sea ice melt, the input of meltwater dilutes total alkalinity and dissolved inorganic carbon—thereby lowering the partial pressure of CO_2 (pCO_2) in seawater, e.g., [17–19]. Meltwater also enhances the water column stratification [20], which limits the vertical mixing of CO_2-rich subsurface waters. The combined influence of these physical, chemical, and biological processes determines whether the Arctic surface waters act as a net CO_2 sink or source during the melt season.

These physical, chemical, and biological interactions are particularly evident during the seasonal freeze-melt cycles of sea ice, which influence the pCO_2 in surface seawater [21]. During sea ice formation, brine rejection releases CO_2-supersaturated brine into the water column, raising surface seawater pCO_2 [21,22]. Under-ice seawater mixing and heightened local respiration from heterotrophic activity [21] can further amplify this increase. pCO_2 commonly peaks its annual maximum in winter, although it does not necessarily exceed atmospheric levels, e.g., [18,23]. Conversely, during sea ice melt, the inputs of CO_2-depleted meltwater [24], the potential for dissolution of ikaite crystals [25], and CO_2 uptake by algae [16,21,26] all contribute to lowering surface seawater pCO_2. Melt ponds can further influence under-ice seawater pCO_2 [27]. As sea ice warms in spring, brine volume increases, and melt pond water that has been in contact with the atmosphere drains through cracks or brine channels in the ice [28] hereby affecting pCO_2 in under-ice seawater [27].

The number of carbonate system measurements in the Arctic Ocean has grown significantly in recent years [29]; however, high-frequency measurements of pCO_2 in under-ice seawater during the melt period remain limited. To date, only one such study has been conducted, focused on a shallow coastal area in Svalbard [30]. This scarcity reflects the logistical and environmental challenges of collecting high-frequency data in remote and harsh Arctic environments. As Arctic warming continues and summer sea ice melt intensifies, it becomes relevant to understand how melt-driven processes influence pCO_2 dynamics in the seawater.

In this study, we investigate the role of snow and sea ice melt, melt pond water drainage, seawater mixing, and primary production in driving pCO_2 variability during the summer thaw. Using a unique, high-frequency dataset of pCO_2, salinity, and temperature collected at 2.5 m below the snow-covered sea ice—complemented by carbonate chemistry measurements in snow, sea ice, and seawater over a 30-day melt period—we provide new insights into processes driving pCO_2 reduction, which is crucial for understanding the CO_2 uptake capacity of surface seawater after sea ice breaks up.

2. Regional Settings

The Young Sound-Tyrolerfjord (YS; 74° N) is a ca. 90 km long sill fjord located in Northeast Greenland (Figure 1). The fjord is 2–7 km wide, covers 390 km^2, and has a mean depth of 100 m [31]. Landfast sea ice typically covers the fjord for 9–10 months each year, from September/October to mid–July [31]. Seasonal sea ice formation and melt, together with exchange with the coastal ocean, strongly modify seawater characteristics in YS. During autumn and winter, brine rejection during sea ice formation contributes to the mixing of the water column, whereas in spring and summer, sea ice melt promotes stratification [32]. Freshwater runoff reaches the fjord from multiple catchments (total area ~3100 km^2) that include vegetated and non-vegetated terrain and land-terminating glaciers [33], with the Zackenberg river being the dominant source and peaking in July [33]. In our study period, the river began discharging on 9 June, after the onset of the sea ice and snow melt. Melt ponds—mixtures of snow and sea ice meltwater—also freshen the

surface layer and lower salinity, e.g., [24]. The fjord has a tidal regime governed by the M2 constituent, and a tidal range that varies between 0.8 and 1.5 m [31]. A shallow sill (50 m) at the fjord mouth limits exchange of deep waters between YS and the Greenland Sea.

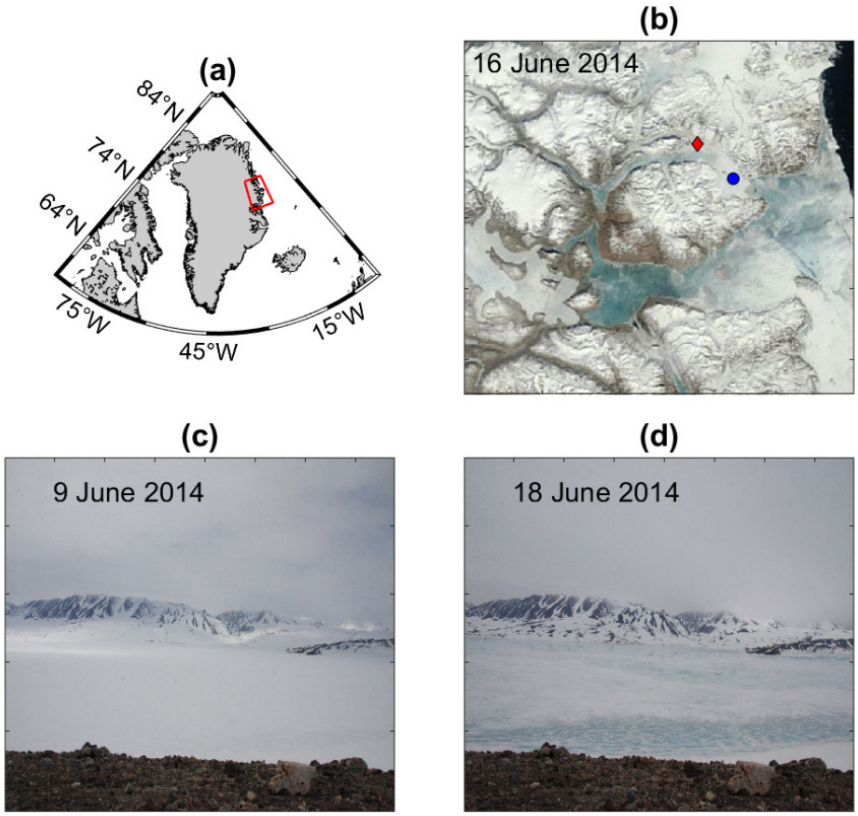

Figure 1. (**a**) Study area in Young Sound-Tyrolerfjord, Northeast Greenland (74° N, 20° E), indicated by the red box. (**b**) Satellite image from 16 June 2014 (Landsat 8), showcasing the fjord's sea ice and snow cover at the time of the field campaign. The blue dot on this image highlights the under-ice sampling location of the CONTROS HydroC® CO_2 and SBE37SM. The red diamond represents the outlet location of Zackenberg river. (**c**,**d**) Time lapse photographs capturing onset of sea ice melt (9 June 2014) and the formation of melt ponds on the sea ice's surface (18 June 2014).

3. Material and Methods

3.1. Sampling

3.1.1. Discrete CTD Profile Measurements

Seawater temperature and salinity throughout the water column were measured through ice holes with a Temperature–Conductivity–Depth (CTD) Seabird SBE19+ (Sea-Bird Scientific, Bellevue, Washington, USA) profiler in May and June 2014. Absolute salinity (SA) and conservative temperature (CT) were computed using the state equation TEOS-10 [34].

3.1.2. Continuous Measurements of SA, CT, and pCO_2

SA and CT, as well as the partial pressure of CO_2 (pCO_2 in µatm), were measured continuously, at 0.2 Hz frequency, at roughly 2.5 m below the sea ice surface (Figure 1b) between 1 and 30 June 2014. The reported values represent the average of 15 consecutive readings. A Seabird SBE37SM was used for salinity and temperature, while a CONTROS HydroC® CO_2 (4H Jena Engineering, Jena, Germany) was used for the pCO_2 measurements [35]. The measuring range of the sensor HydroC® CO_2 is 100–1000 µatm, with a resolution and initial accuracy of <1 µatm and ± 1% reading, respectively (https://www.4h-jena.de, (accessed on 15 August 2023)). The accuracy of the Seabird SBE37SM is ± 0.003 mS cm^{-1}

for conductivity and ± 0.002 °C for temperature. Calibration of both instruments was performed by their respective supplier before the fieldwork.

3.1.3. Water Isotopes

Oxygen and hydrogen stable isotopes (^{16}O, ^{18}O, ^{1}H, ^{2}H) in seawater were measured at 1, 2.5, 10, 20, 30, 50, and 100 m depths using a Cavity Ringdown Spectrometer, L2130-*I* Isotopic sH_2O (Picarro Inc., Santa Clara, CA, USA). Isotope ratios are reported in δ notation and expressed in per mil (‰) relative to Vienna Standard Ocean Water 2 (VSMOW2) standard, following calibration to the VSMOW2-Standard Light Antarctic Precipitation 2 (SLAP2) scale:

$$\delta^2H = \left(\frac{\frac{^2H}{^1H}_{sample}}{\frac{^2H}{^1H}_{standard}} - 1 \right) \times 1000‰ \quad (1)$$

$$\delta^{18}O = \left(\frac{\frac{^{18}O}{^{16}O}_{sample}}{\frac{^{18}O}{^{16}O}_{standard}} - 1 \right) \times 1000‰ \quad (2)$$

Analytical precision was 0.01‰ for $\delta^{18}O$ and 0.04‰ for δ^2H, calculated as the standard deviation from ten repeated measurements of two different standard materials measured at the beginning and end of each sample set at the University of Manitoba, Winnipeg, Canada. Salinity for each water sample was determined from conductivity (mS cm^{-1}) measured with a meter (Orion 3-star, Thermo Scientific, Waltham, MA, USA) coupled with a conductivity cell (Orion 013610MD, Thermo Scientific) with a precision of ±0.1.

The $\delta^{18}O$—salinity method is commonly used to estimate the meteoric water contribution in the marine environment, e.g., [36–39]. In our study, $\delta^{18}O$ values from melt ponds and snow and sea ice meltwater were used as freshwater endmembers. To discern the dominant meltwater source trough time, we computed the daily intercept ($\delta^{18}O$ at SA = 0) from a linear regression of $\delta^{18}O$ over SA and compared it with (i) melt pond/snow/sea ice endmembers [24] and (ii) $\delta^{18}O$ of local meteoric precipitation in YS estimated with Equation (3) [40]:

$$\delta^{18}O = -0.0051 \times LAT^2 + 0.1805 \times LAT - 0.002 \times ALT - 5.247 \quad (3)$$

where LAT is the latitude (74° N) and ALT is the altitude of Daneborg station (44 m).

Sampling dates with similar potential meltwater sources were grouped based on the visual examination of the intercepts resulting from the linear regression between the $\delta^{18}O$ and SA. The relationship between $\delta^{18}O$ and δ^2H was used to determine the origin of the under-ice seawater during our study. Then, to assess whether the water mass originated within the fjord or was advected from outside, we compared the $\delta^{18}O/\delta^2H$ data with established meteoric water lines, including the Arctic Meteoric Water Line (AMWL, $\delta^2H = 7.6 \times \delta^{18}O - 1.8$, [41]); the Global Meteoric Water Line (GMWL, $\delta^2H = 8.0 \times \delta^{18}O + 10$, [42]); and the Lena River Meteoric Water Line (LRMWL, $\delta^2H = 8.0 \times \delta^{18}O + 6.2$, [41]).

3.1.4. Chlorophyll-a and Nitrate Concentrations

Seawater samples for chlorophyll-a (Chl-a) analysis were collected from 11 to 23 June 2014 at 1 m below the ice cover. Samples were filtered using Whatman GF/C glass-fiber filters and kept frozen in aluminum foil until analysis. At the field laboratory in Daneborg, Greenland, the Chl-a was extracted in 10 mL of acetone at 4 °C for 16 h and measured using a Turner Design TD700 fluorometer (Turner Designs, San Jose, CA, USA).

Nitrate (NO_3^-) concentrations were determined from 50 mL seawater samples collected between 11 and 23 June 2014. Samples were filtered using Whatman GF/C glass-fibre

filters and kept frozen until analysis. NO_3^- was measured using standard colorimetric methods [43], with a 5-cm optical path in a Genesys 10 vis spectrophotometer (Thermo Fisher Scientific, Waltham, Massachusetts, USA). The detection limit was 0.15 µmol L^{-1}. Changes in NO_3^- concentrations over time (ΔNO_3^-) were used to (i) estimate the carbon uptake associated with primary production and (ii) to evaluate the potential role of biological processes in lowering pCO_2 in under-ice seawater. Assuming uptake occurred according to the Redfield C:N ratio of 106:16 [44], ΔNO_3^- values were multiplied by 6.625 to calculate the corresponding dissolved inorganic carbon removal (ΔDIC_{pp}). The cumulative ΔDIC_{pp} over the study period was then used as a proxy for the total amount of carbon consumed by primary producers.

3.1.5. Total Alkalinity and Dissolved Inorganic Carbon

The total alkalinity (TA) and dissolved inorganic carbon (DIC) samples were collected between 2 and 24 June 2014 in under-ice seawater at 2.5 m. The samples were collected in gas-tight vials (12 mL Exetainer, Labco High Wycombe, UK). To preserve the samples, a 12 µL solution of saturated mercury chloride was added, and the vials were subsequently stored in the dark at room temperature until analysis.

TA was determined by Gran titration [45] using a TIM 840 titration system (Radiometer Analytical, ATS Scientific, Burlington, Ontario, Canada). This system comprised a Ross sure-flow combination pH glass electrode (Orion 8172BNWP, Thermo Scientific) and a temperature probe (Radiometer Analytical, Lyon, France). Samples were titrated with a standard 0.05 M HCl solution (Alfa Aesar, Haverhill, MA, USA). DIC was measured on a DIC analyzer (Apollo SciTech, Newark, DE, USA). This analysis involved the acidification of a 0.75 mL subsample with 1 mL 10% H_3PO_4 (Sigma-Aldrich, Saint-Louis, MO, USA), and the subsequent quantification of the released CO_2 with a nondispersive infrared CO_2 analyzer (LI-COR, LI-7000, Lincoln, NE, USA). The results were then converted from µmol L^{-1} to µmol kg^{-1} based on sample density, estimated from salinity and temperature at the time of the analysis. Accuracies of ±3 and ±2 µmol kg^{-1} were determined for TA and DIC, respectively, from routine analysis of certified reference materials (A.G. Dickson, Scripps Institution of Oceanography, San Diego, CA, USA).

3.2. Data Analysis

3.2.1. Calculated pCO_2 Based on TA and DIC

Seawater pCO_2 (in µatm) was calculated by the CO2SYS program version 01.05 [46] using the in situ temperature, salinity, TA, and DIC, coupled with the dissociation constants from [47] refitted by [48]. These constants were chosen because previous studies in Arctic waters showed a good alignment with both measured and calculated values [49,50]. The pCO_2 in Zackenberg river was calculated by the same program, using the TA and pH (NBS scale) collected by the Greenland Ecosystem Monitoring program (GEM) on 4 June 2014 (http://data.g-e-m.dk, (accessed on 4 September 2023)).

3.2.2. Estimates of Fraction of Freshwater

To quantify the fraction of freshwater, f_{fw}, in under-ice seawater over time, we used the following equation:

$$f_{fw} = 1 - \frac{S_{meas}}{S_{ref}} \quad (4)$$

where S_{meas} is the measured salinity (SA) and S_{ref} is the reference salinity in the under-ice seawater. S_{ref} corresponds to seawater salinity before the onset of snow and sea ice melt. It serves as a baseline for comparing seawater conditions before and after snow and sea ice start to melt.

3.2.3. Estimates of pCO_2 Uptake by Primary Production

The contribution of primary production (PP) to the pCO_2 uptake, is estimated from the daily carbon consumption by the photosynthetic community, using the primary productivity/Chl-a ratio (5.6 C d^{-1}) from YS. This ratio is a literature-derived value, determined from maximum primary productivity and Chl-a values recorded in YS between June and August 1996 (10 µg C $L^{-1}d^{-1}$ and 1.8 µg L^{-1}, respectively [51]). Subsequently, the carbon consumed by PP (µg C L^{-1} d^{-1}) during our study was calculated as the product of primary productivity/Chl-a ratio (C d^{-1}) and the maximum Chl-a (µg L^{-1}) in under-ice seawater in YS during June 2014. Maximum Chl-a values were used to capture the potential maximum CO_2 uptake by PP in YS during our study period.

3.2.4. Effects of Snow and Sea Ice Meltwater Mixing on Under-Ice pCO_2

To quantify the effect of meltwater inputs on carbonate system properties, we estimated the conservative mixing value for each property X ∈ {SA, CT, TA, DIC} following Equation (5):

$$X_{mix} = \frac{(X_i \times L_i) + (X_w \times L_w)}{(L_i + L_w)} \quad (5)$$

where X_{mix} is the conservative mixing value of each property (SA_{mix}, CT_{mix}, TA_{mix}, DIC_{mix}), X_i and X_w denote the property values in meltwater (snow or sea ice) and in the under-ice seawater, respectively. L_i represents the decrease in meltwater layer thickness (snow or sea ice) over the study period—extracted from Table 1 in [24], which reports in situ measurements obtained during the same sampling campaign. L_w represents the thickness of the under-ice seawater (i.e., the mixed layer depth). The mixed layer depth L_w was estimated from density profiles and defined as the depth where density increased by 0.01 kg m^{-3}. This threshold is typical for the Arctic region [52–55].

Table 1. End-member values for snow meltwater and melt pond water, showing measured data and values estimated from the linear regression model.

Freshwater Source	Measured $\delta^{18}O$ (‰)	$\delta^{18}O$ at SA = 0 (‰)
Snow meltwater	−19.1 [a]	−19.9
Melt pond water	−13.6 [b]	−12.5

[a] Value calculated using Equation (3). [b] Value taken from [24].

Equation (5) accounts for freshwater driven processes that affect carbonate chemistry, including brine dilution due to sea ice melt, and ikaite dissolution, as well as biological processes such as CO_2 uptake by primary producers.

Afterwards, we calculated the pCO_2 under mixing conditions as following: $pCO_{2_{mix}}$ = CO2SYS (SA_{mix}, CT_{mix}, TA_{mix}, DIC_{mix}).

Additionally, to evaluate whether conservative-mixing (dilution) can explain the observed pCO_2 decrease, we compare our measured DIC values to a fixed-atmosphere baseline. We computed the DIC consistent with a reference pCO_2 = 401 µatm using the CO2SYS and then form the conservative expectations at fixed pCO_2:

$$DIC_{401,sw} = CO2SYS(SA, CT, TA_{mix}, pCO_2 = 401) \quad (6)$$

$$TA_{mix} = (1 - f_{fw}) \times TA_{sw} + f_{fw} \times TA_{mw} \quad (7)$$

$$DIC_{401,mix} = (1 - f_{fw}) \times DIC_{401,sw} + f_{fw} \times DIC_{mw} \quad (8)$$

where f_{fw} is the freshwater fraction derived from salinity from Equation (4), *mw* is the snow or sea ice end-member, '*mix*' denotes the conservative value from the salinity-defined end-member line [56], and the subscript *sw* for seawater (measured values).

Because TA is not strictly conservative in sea ice-influenced waters, ikaite precipitation within sea ice and dissolution during melt modify TA and pCO_2 in the underlying seawater [25], we (i) normalize TA and DIC to salinity (nTA, nDIC) and (ii) quantify departures from conservative mixing using residuals defined as:

$$\Delta TA = TA_{sw} - TA_{mix} \quad (9)$$

$$\Delta DIC = DIC_{sw} - DIC_{401,mix,TA_{mix}} \quad (10)$$

3.2.5. Pearson Correlation

The time series was split into three sections based on changes of the Pearson correlation coefficients calculated for the relationship among pCO_2, SA, CT, and the CT-SA correlation. Temporal changes in the correlation coefficients, combined with shifts in potential meltwater sources, were used to classify the distinct periods throughout our sampling.

4. Results

4.1. Hydrographic Conditions

Vertical profiles of SA and CT show a well-mixed water column in the upper 30 m on May 15 with SA of 32.38 g kg^{-1} and CT at near freezing point of −1.75 °C (Figure 2a,b). These profiles are representative of the hydrographic settings before the onset of snow and sea ice melt. By the end of May, SA decreased in the upper 30 m with the lowest values at the sea surface (SA = 32.19 g kg^{-1}), while CT increased to −1.68 °C/−1.65 °C, reflecting the onset of snow and sea ice melt. These changes in SA and CT resulted in a stratified water column (Figure 2c).

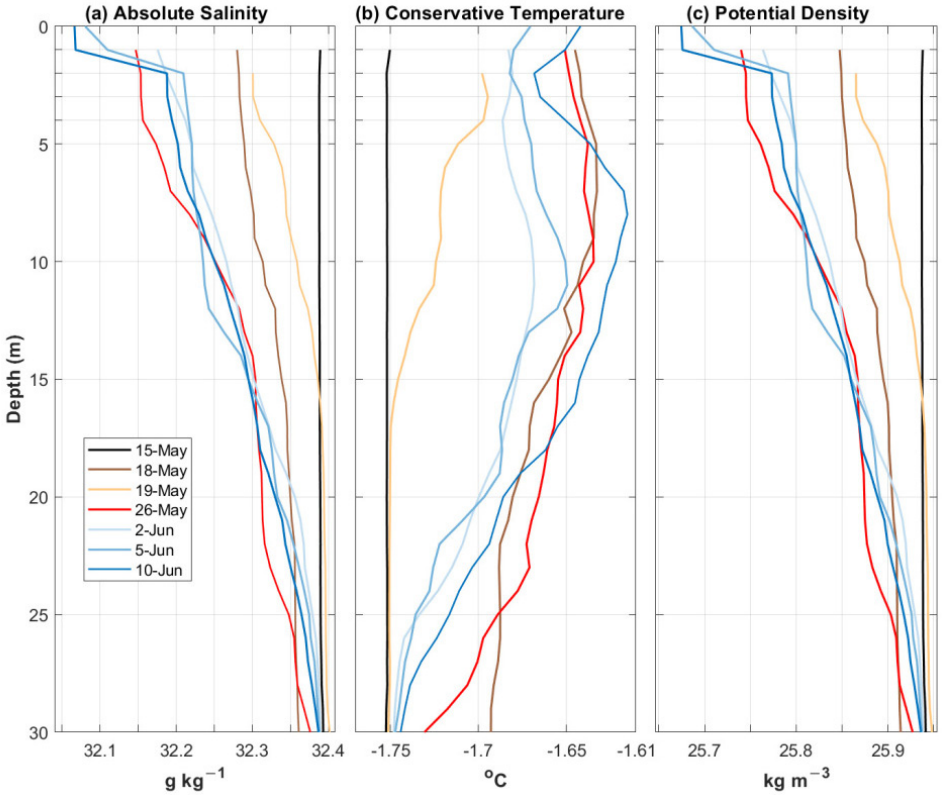

Figure 2. Vertical profiles of (**a**) absolute salinity, (**b**) conservative temperature, and (**c**) potential density.

4.2. Atmospheric Temperature and Snow and Sea Ice Conditions

Air temperatures increased steadily from below 0 °C to 10 °C between 1 and 11 June (Figure 3a). From 11 to 18 June, temperatures ranged between 4 °C and 14 °C, and melt ponds started to form on the sea ice surface (Figure 1c,d), resulting in a decrease in snow thickness (from 60 cm to 14 cm). After 18 June, temperatures dropped and remained around 0 °C. By the end of June, temperatures increased to about 5 °C. While these fluctuations in air temperatures resulted in a thinning of the snow cover, the sea ice thickness remained relatively stable, decreasing from 145 cm to 135 cm throughout the survey [24]. Based on in situ sea ice temperature and salinity, the calculated brine volume fraction remained above the permeability threshold of 5% [57] or 7% [58] suggesting that the ice cover was permeable [24].

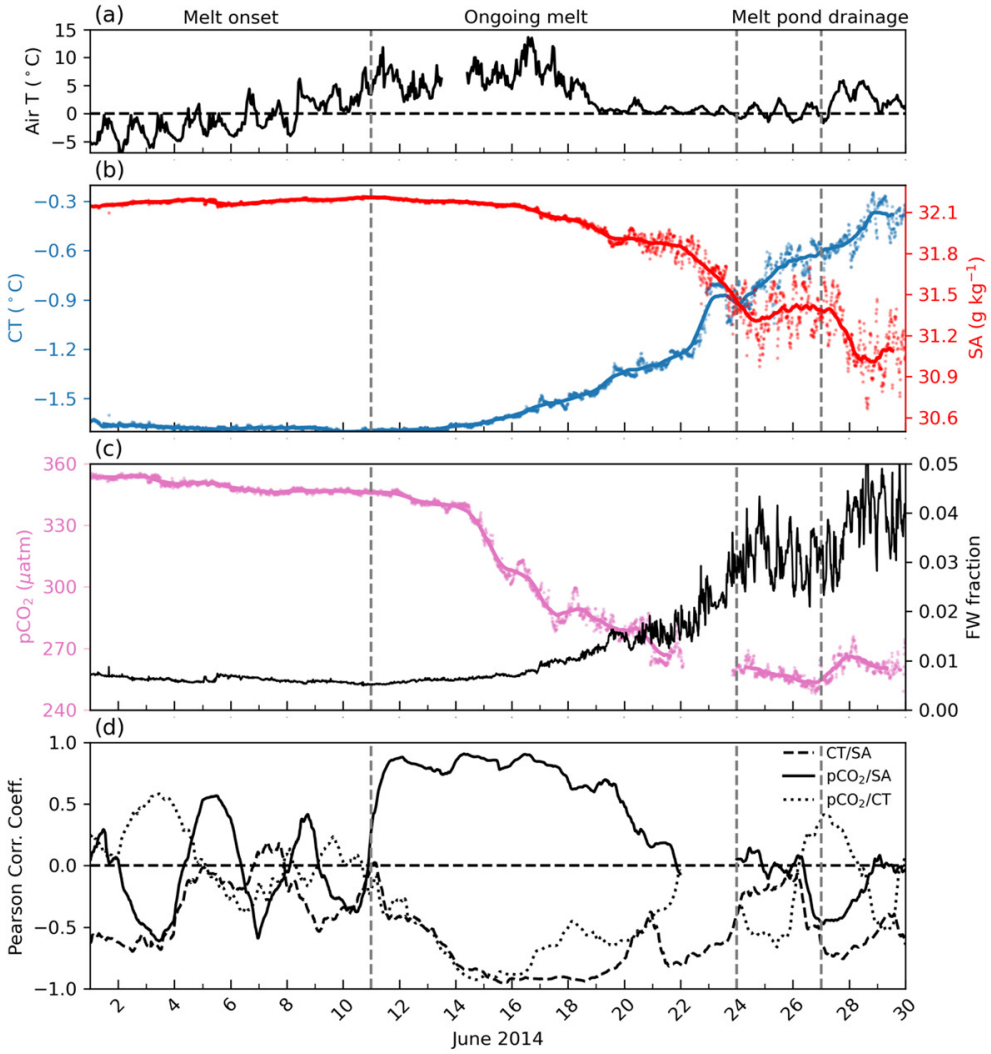

Figure 3. Time series in under-ice seawater (2.5 m) separated by three periods: melt onset, ongoing melt, and melt pond drainage: (**a**) air temperature (Air T), (**b**) conservative temperature (CT; blue) and absolute salinity (SA; red), (**c**) pCO_2 (pink) and freshwater fraction (FWfraction; black). Dots represent raw data, whereas continuous lines represent the average values on a one-day window. (**d**) Pearson correlation coefficients between CT and SA (dashed line), pCO_2 and SA (solid line), and pCO_2 and CT (dotted line). For CT and SA, n = 2898 and for pCO_2, n = 2714. Vertical dashed grey lines correspond to changes of periods (melt onset, ongoing melt, and melt pond drainage) based on the calculated changes on the Pearson coefficients.

4.3. Continuous Measurements of SA, CT, and pCO_2

From 1 to 10 June, SA and CT remained relatively constant, ranging from 32.09 g kg^{-1} to 32.20 g kg^{-1} (mean = 32.17 g kg^{-1}, SD = 0.01 g kg^{-1}) and from −1.60 °C to −1.71 °C (mean −1.67 °C, SD = 0.01 °C), respectively. The seawater pCO_2 was undersaturated compared to the atmosphere (401 µatm), slightly decreasing from 353.6 to 346.2 µatm (mean = 350.5 µatm, SD = 3.4 µatm, Figure 3c). The Pearson correlation between CT and SA exhibited sharp fluctuations over time (from −0.5 to 0), indicating that CT and SA lacked any discernible pattern to seawater properties (Figure 3d). After 11 June, SA decreased from 32.19 g kg^{-1} to 31.56 g kg^{-1} and CT increased from −1.70 °C to −0.95 °C. A strong Pearson correlation between CT and SA (−0.97) suggests that changes in these variables are associated from the same process (Figure 3d). Seawater pCO_2 decreased from 344.9 µatm to 261.4 µatm (Figure 3c), associated with decreasing SA and increasing CT (Pearson correlation of 0.87 and −0.90, respectively), suggesting that fresher and warmer water contributed to lowering the pCO_2. Between 24 and 27 June, an overall increase in CT (from −0.82 °C to −0.55 °C) and a decrease in SA (from 31.43 g kg^{-1} to 31.25 g kg^{-1}) was observed while both variables exhibit high local maxima and minima due to enhanced stratification (Figure 3b). Likewise, seawater pCO_2 decreased slightly to 248 µatm. During this period, the Pearson correlations between pCO_2 and SA and CT and SA were near zero, while the correlation between pCO_2 and CT increased to −0.55. This suggests that the observed pCO_2 changes were due to the intrusion of warm seawater. From 28 to 30 June, pCO_2 stabilized at around 261 µatm.

4.4. Water Isotopes

The observed $\delta^{18}O$ of seawater was correlated with SA, with $\delta^{18}O$ values ranging from -2.9‰ to −1.0‰ (Figure 4a). However, early in the survey (1–10 June), $\delta^{18}O$ values were closely clustered without a clear pattern or significant correlation, suggesting the remnant influence of spring convection (Figure 4a). During this period, the data primarily aligned with the Lena River Meteoric Water Line (LRMWL), indicating that the under-ice seawater was sourced predominantly from outside the fjord (Figure 4b). Between 11 and 21 June, a clear negative relationship between $\delta^{18}O$ and SA emerged as shown by the r^2-value of 0.8 (Figure 4a), and the data deviated from LRMWL toward the Arctic Meteoric Water Line (AMWL; Figure 4b). The $\delta^{18}O$ intercept of −19.9‰, which is consistent with local precipitation (−19.1‰, Table 1), suggests that snowmelt contributed to the freshening of the under-ice seawater. By 24 June, the negative relationship between $\delta^{18}O$ and SA persisted, with the $\delta^{18}O$ intercept shifting to -12.5‰, closer to the values observed in melt ponds (−13.6‰, Table 1). This suggests that the under-ice seawater was influenced by the drainage of melt pond water, derived from snow and sea ice melt (Figure 4a). This assumption is consistent with the observed deviation from the AMWL toward the LRMWL, indicating advection of water from outside the fjord, which carried the signature of melt ponds (Figure 4b).

4.5. Chlorophyll-a and Nitrate Concentrations

Chl-a and NO_3^- concentration varied from 0.01 to 0.66 µg L^{-1} and from 0 to 2.2 µmol L^{-1}, respectively. From 17 June onward, the under-ice seawater remained NO_3^--depleted (Table 2).

Table 2. Chlorophyll-a (Chl-a) and nitrate (NO_3^- concentration at 1 m in the under-ice seawater.

Date (2014)	Chl-a (μg L^{-1})	NO_3^- (μmol L^{-1})
11 June	0.01	2.20
17 June	0.66	0.00
23 June	0.12	0.00

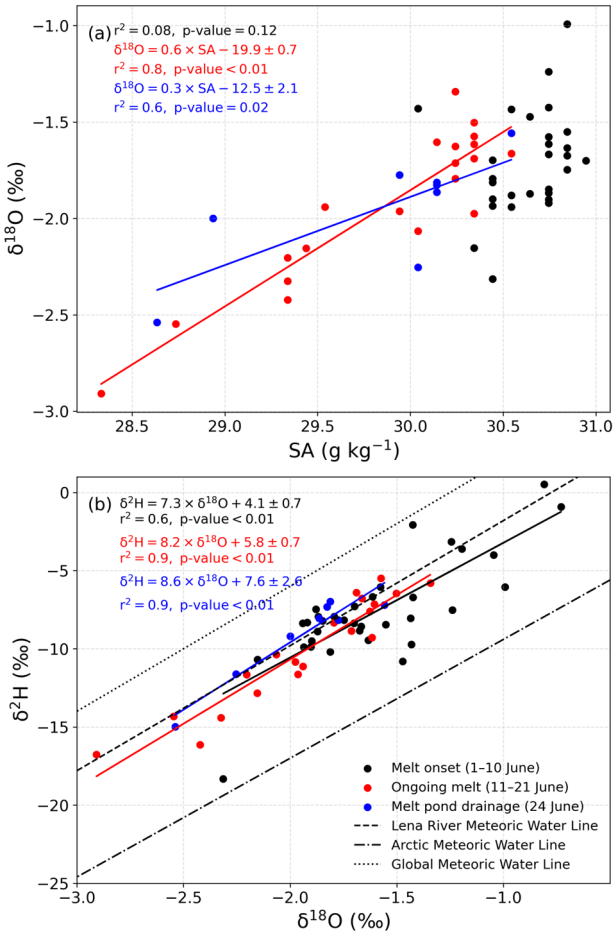

Figure 4. (**a**) The $\delta^{18}O$ (‰) values as a function of absolute salinity (SA) for the melt onset period (black dots, n = 28), ongoing melt (red dots, n = 20), and drainage of melt pond water (blue dots, n = 8). (**b**) The δ^2H (‰) as a function of $\delta^{18}O$ (‰) values. The dashed, dash-dotted, and dotted lines indicate potential sources of meteoric water for the under-ice seawater in YS.

5. Discussion

The under-ice seawater pCO_2 was undersaturated (248–354 μatm) compared to the atmosphere (401 μatm), suggesting that seawater had the potential to act as a sink for atmospheric CO_2. While the underlying seawater was initially undersaturated (354 μatm) compared to the atmosphere, the input of meltwater derived from snow and sea ice results in a further reduced seawater pCO_2 to 248 μatm. To elucidate the mechanisms driving these changes, a range of physical and biological processes were investigated for their potential influence on seawater pCO_2 dynamics.

5.1. Melt Onset Caused a pCO_2 Decrease in Under-Ice Seawater

Discrete observations between 15 May and 29 May, revealed the formation of a layer with relatively low salinity (SA < 32.20 g kg^{-1}) and high temperature (CT = −1.65 °C)

at the seawater surface (Figure 2a,b), indicating an influx of fresh water that marked the beginning of the melt season. Afterwards, the time series data show that from 1 to 10 June, SA and CT remained relatively constant (Figure 3b), and no significant inputs of fresh meltwater were detected (Figure 4a), suggesting only subtle signs of snow and sea ice melt at this early stage. The $\delta^2H-\delta^{18}O$ data lie on the LRMWL, indicating that the under-ice seawater was predominantly sourced from outside the fjord (Figure 4b). This fresh meltwater inflow triggered a subtle yet steady decrease in seawater pCO_2 (~8 µatm; Figure 3c).

5.2. Snow and Sea Ice Melt Reduce pCO_2 in Under-Ice Seawater

Between 11 and 24 June, seawater pCO_2 decreased by 84 µatm. This decline was strongly correlated with the presence of fresher, warmer waters, suggesting that meltwater mixing caused the observed drop in seawater pCO_2 (Figure 3d). To isolate the primary driver of the pCO_2 decrease, we examined and excluded other potential contributing processes.

Vertical mixing with deeper water was ruled out as a possible explanation. Using measured SA, CT, TA, and DIC at 10 m, we calculated a pCO_2 of 370 µatm (Table 3). In the conservative mixing model—based on SA, CT, TA, and DIC—it would require ca. 90% of deeper water to be mixed with the surface layer to reach a pCO_2 of 370 µatm. This scenario is unlikely given the stratified conditions (Figure 2c). Moreover, such mixing would increase, rather than decrease, pCO_2 beneath the ice.

Table 3. End-member values for absolute salinity (SA), conservative temperature (CT), total alkalinity (TA), dissolved inorganic carbon (DIC), pH, and calculated pCO_2 (pCO_2_calc) in surface water, deep water, Zackenberg river, snow and sea ice meltwater, and in the atmosphere.

Source	SA	CT	TA	DIC	pH	pCO_2_Calc [e]	pCO_2
	(g kg^{-1})	(°C)	(µmol kg^{-1})	(µmol kg^{-1})	(NBS)	(µatm)	(µatm)
Surface water [a]	32.2	−1.7	2222	2114		344	
Deeper water [b]	32.3	−1.7	2217	2119		370	
Zack. River [c]	0	0.2	280	447 [e]	6.6	2174	
Snow Meltwater [d]	0	0	52	44		1	
Sea ice Meltwater [d]	4.8	−1.7	378	364		45	
Atmosphere							401

[a] Collected at 2.5 m depth on 2 June. [b] Collected at 10 m depth on 2 June. [c] Data collected on 4 June 2014 gathered from GEM database. [d] Samples were collected during May and June 2014 [24]. [e] Calculated value from CO2SYS.

Freshwater inputs from precipitation and river runoff were also considered. Precipitation during the study period totaled just 4.1 mm and resulted in a negligible decrease of only 0.4 µatm in under-ice seawater pCO_2. Similarly, runoff—primarily from the melting of the snow and glacial ice [33]—is unlikely to explain the observed pCO_2 reduction. Using measured TA and pH, we estimate river water pCO_2 up to 2174 µatm (Table 3). With a f_{fw} of 0.02 at most during the ongoing melt, mixing of river water results in pCO_2 of 342 µatm, indicating a negligible effect on under-ice pCO_2 (Table 4).

The observed decrease in under-ice pCO_2 is best explained by dilution from mixing with meltwater from snow and sea ice. Under conservative mixing, the addition of meltwater—low in TA and DIC—reduces TA and DIC as salinity falls, which in turn lowers pCO_2. We isolated the role of mixing by computing a DIC at a fixed pCO_2 of 401 µatm and compared measured DIC (DIC_{sw}) and TA (TA_{sw}) with their conservative-mixing ex-

pectations ($DIC_{401,mix}$ and TA_{mix}). Measured values fall near the 1:1 line (Figure 5a,b), showing that most of the variability in DIC_{sw} and TA_{sw} can be reproduced by simple dilution with meltwater, without invoking additional reactions. After removing the dilution, dissolution, photosynthesis, and CO_2 release leave a fingerprint (Figure 5c,d). Calcium carbonate ($CaCO_3$) dissolution is expected as melting continues, because sea ice contains $CaCO_3$—in the form of ikaite—that dissolve upon mixing, adding proportionally more TA than DIC and thereby further lowering the under-ice pCO_2, cf. [25]. Mixing also modifies the carbonate buffer balance. As SA decreased, the TA/DIC ratio increased (Figure 5e), indicating stronger dilution of DIC than TA. This shift raises the buffering capacity and lowers pCO_2. A strong negative correlation between the TA/DIC ratio and measured pCO_2 further supports this mechanism (Figure 5f).

Table 4. Results from the mixing of snow or sea ice meltwater with the under-ice seawater. L_w denotes the under-ice seawater layer, and L_i represents the decrease in meltwater layer thickness (snow or sea ice). Reported parameters include the mixed absolute salinity (SA_{mix}), mixed conservative temperature (CT_{mix}), mixed total alkalinity (TA_{mix}), mixed dissolved inorganic carbon (DIC_{mix}), mixed pCO_2 (pCO_{2mix}), and ΔpCO_2.

Scenario	L_w (m)	L_i [e] (m)	SA_{mix} [a] (g kg^{-1})	CT_{mix} [a] (°C)	TA_{mix} [a] (µmol kg^{-1})	DIC_{mix} [a] (µmol kg^{-1})	pCO_{2mix} [b] (µatm)	ΔpCO_2 [c] (µatm)
Snow meltwater mixed with seawater	2.5	0.36	28.1	−1.5	1949	1853	285	59
Sea ice meltwater mixed with seawater	2.5	0.1	31.1	−1.7	2151	2047	320	24
River water mixed with seawater [d]			31.6	−1.7	2183	2081	342	2

[a] Calculated values from Equation (5). [b] Calculated values from CO2SYS (Section 3.2.4). [c] $\Delta pCO_2 = pCO_{2_{mix}} - pCO_{2_{calc}}$ [d] Calculated using Equation (7). [e] Layer thickness measurements were obtained from [24].

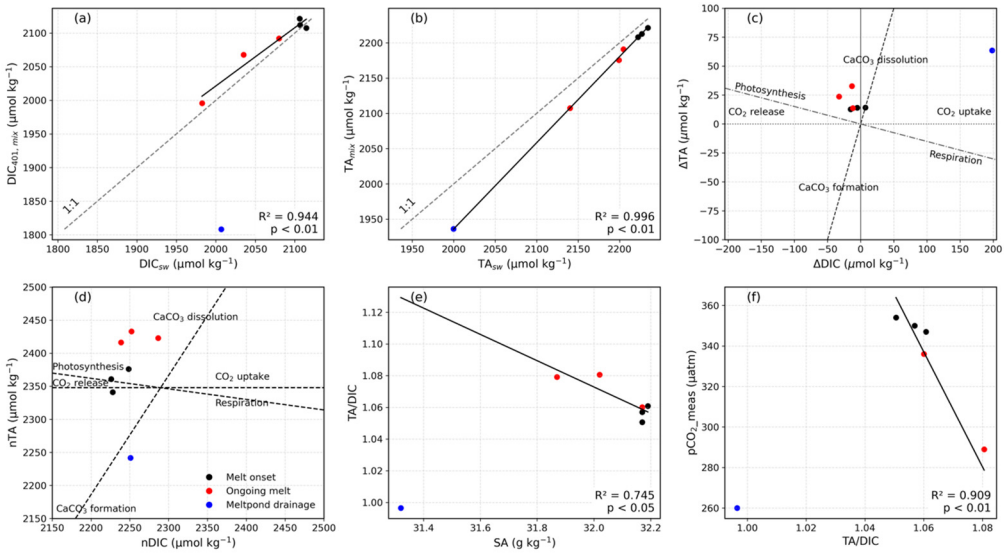

Figure 5. Relationships between (**a**) measured DIC (DIC_{sw}) and $DIC_{401,mix}$, (**b**) measured TA (TA_{sw}) and TA_{mix}, (**c**) DIC (ΔDIC) and TA residual (ΔTA), (**d**) nDIC and nTA (normalized at S_{ref} = 32.38 g kg^{-1}). The different dashed lines in panel (**c**,**d**) represent the theoretical evolution of nTA/nDIC ratio and residuals following the precipitation/dissolution of calcium carbonate, release/uptake of CO_2(g) and biological photosynthesis/respiration. (**e**) Relationship between the TA/DIC ratio and SA (g kg^{-1}), and (**f**) between the TA/DIC ratio and measured pCO_2 (pCO_2_meas).

Using the SA_{mix}, CT_{mix}, TA_{mix}, DIC_{mix}, the conservative-mixing calculation attributes pCO_2 reductions of 59 µatm (snow) and 24 µatm (sea ice) within the upper 2.5 m of the water column (Table 4)—together sufficient to explain the observed decline in pCO_2. Our findings that meltwater mixing reduce pCO_2 align with prior work showing that low-salinity, TA, and DIC meltwater mixed with saline fjord water with high TA and DIC drives pCO_2 undersaturation via the salinity dependent, nonlinear carbonate system in Godthåbsfjord, Southwest Greenland [18] and with recent melt pond observations in the central Arctic Ocean, reporting strong pCO_2 reduction from meltwater pond-seawater mixing [59].

5.3. Drainage of Melt Pond Water Affects pCO_2 in Under-Ice Seawater

By mid-June, with seasonal increases in air temperature (Figure 3a), snow thickness diminished [24], leading to the accumulation of meltwater on the surface of the sea ice (Figure 1d). The warming of the sea ice increased its permeability, cf. [28], providing a direct pathway for meltwater drainage into the underlying seawater. After June 22, seawater temperatures rose significantly (CT > −1.25 °C) and salinity decreased (SA < 32 g kg^{-1}), resulting in a twofold increase in the freshwater fraction (Figure 3b,c). This suggests that freshwater inputs from melt pond drainage were occurring. Consistent with this, the intercept of the δ^{18}O-SA regression in seawater (−12.5‰; Figure 4a; Table 1) closely aligns with that of melt pond water (−13.6‰, Table 1), indicating that melt ponds were the primary source of fresher water during this period. As the melt season progressed, the heat-absorbing capacity of the meltwater ponds exceeded that of the surrounding sea ice and snow, cf. [60], resulting in a rise in seawater CT and a decline in pCO_2 in the under-ice seawater (correlation coefficient = −0.5; Figure 3d). This decline was particularly evident between June 24 and 27, when pCO_2 in the under-ice seawater dropped to 248 µatm, driven by mixing of meltwater ponds with low salinity, TA, and DIC [59]. The drainage of meltwater pond into the under-ice seawater occurred through tidal sea ice cracks or directly percolating through brine channels into the under-ice seawater, altering the nDIC/nTA relationship (Figure 5c,d). Thus, the drainage of melt ponds effectively facilitated the connection between the ocean and atmosphere in late spring despite the presence of sea ice cover, ultimately decreasing pCO_2 in the under-ice seawater. Consequently, meltwater input at this stage of melt enhances the capacity of seawater to uptake atmospheric CO_2.

5.4. pCO_2 Uptake by PP in Under-Ice Seawater

Biological drawdown of pCO_2 was also considered, as PP contributed to the decrease of pCO_2 during the development of under-ice blooms [16,26,61,62]. Our findings indicate an estimated carbon uptake of approximately 9 µmol kg^{-1} during the study period (see Section 3.2.3). This corresponds to a maximum reduction of 25 µatm of pCO_2 over the 30-day melt period from 1 June to 30 June. As an independent approach, we also estimated the potential DIC consumption by PP based on NO_3^- concentrations measured in the under-ice seawater (Table 2). This indicate a cumulative DIC uptake due to PP (ΔDIC_{pp}) of approximately 14.6 µmol L^{-1}—which is comparable to the values derived from the maximum Chl-a concentration—and supports our interpretation that PP made only a modest contribution (23%) to the pCO_2 reduction. Our finding of only modest uptake of pCO_2 by PP is consistent with observations from west Greenland fjords influenced by land-terminating glaciers, where low-surface water NO_3^- constrains PP and hence biological CO_2 uptake [63]. Similarly, in YS, the low nutrient content of Polar Water [64,65] suppresses bloom development, reinforcing the limited role of PP in controlling under-ice pCO_2.

5.5. Comparison Between Measured and Calculated pCO_2 in the Under-Ice Seawater

The observed differences between measured (pCO_2_meas) and calculated pCO_2 (pCO_2_calc) in under-ice seawater appear to be influenced by processes related to snow

and sea ice melt. Until 21 June, a strong relationship (r^2-value = 0.9) is evident between pCO_2_meas and pCO_2_calc values (Figure 6), suggesting that carbonate chemistry is well constrained by the measured TA and DIC. However, this relationship breaks down on 24 June, coinciding with the signal of meltwater ponds in the under-ice seawater (Figure 4a). One explanation of this shift lies in the timing and mechanisms of ion release from sea ice, particularly from brine inclusions [66]. During warming brine and carbonate ions percolate from the sea ice into the underlying seawater. The timing and intensity of this ion release can strongly alter carbonate chemistry by modifying TA and DIC independently, which in turn affects calculated pCO_2 [59]. If the carbonate system is out of equilibrium during rapid meltwater input, discrepancies between measured and calculated pCO_2 are expected. Discrepancies have been previously detected in YS and seem to be related to sea ice processes.

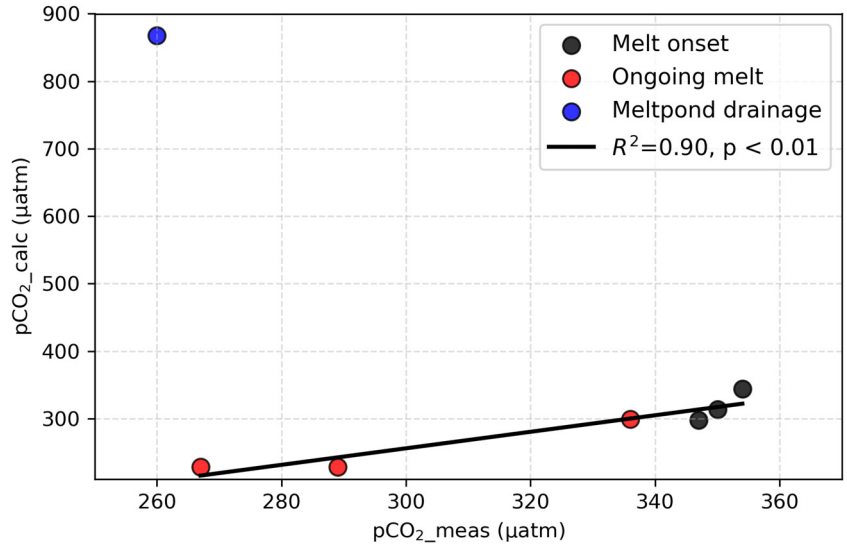

Figure 6. Relationship between calculated pCO_2 (pCO_2_calc) and measured pCO_2 using the CO2SYS program and HydroC® CO_2 sensor, respectively.

6. Conclusions

- This study provides data on the few continuous, high-resolution measurements of pCO_2 in under-ice seawater, capturing the transition from melt onset to melt pond drainage in Young Sound-Tyrolerfjord, Northeast Greenland.
- We demonstrated that dilution from mixing with meltwater from snow and sea ice was the primary driver of the observed pCO_2 decline in the under-ice seawater.
- The subsequent drainage of melt ponds through the ice as the melting season progressed marked the onset of the connection between the atmosphere and the under-ice seawater despite persistent snow and sea ice cover.
- This connection establishes pathways for gas exchange between the atmosphere and under-ice seawater, even before sea ice breakup.
- Primary production played a secondary role in this pCO_2 reduction, compared to dilution from snow and sea ice melt.
- High-frequency under-ice pCO_2 measurements enabled us to capture rapid variability and revealed systematic discrepancies between measured and calculated pCO_2, pointing to limitations of relying solely on calculated values in sea ice-influenced coastal waters.
- Our findings enhance the understanding of how meltwater influences surface-water pCO_2 dynamics in Arctic coastal waters and highlight their importance for predicting the future oceanic uptake of atmospheric CO_2 under continued sea ice decline.

Author Contributions: Conceptualization, J.V., S.R. and E.R.-C.; data collection, S.R., N.-X.G., W.B., T.P. and L.L.S.; formal analysis, J.V.; data curation, J.V., E.R.-C. and W.B.; writing—original draft preparation, J.V.; writing—review and editing, J.V., S.R., E.R.-C., N.-X.G., W.B., T.P. and L.L.S.; visualization, J.V. and E.R.-C.; funding acquisition, S.R. and L.L.S. All authors have read and agreed to the published version of the manuscript.

Funding: This research received financial support from the Arctic Research Centre, Aarhus University, the Aage V. Jensens Foundations (Grant No. 30122021), NSERC, the Canada Excellence Research Chair program (S. Rysgaard), and the Danish National Research Foundation (grant #DNRF 185) (S. Rysgaard).

Data Availability Statement: The dataset of high-frequency measurements of pCO_2, temperature, and salinity is available in https://doi.pangaea.de/10.1594/PANGAEA.969461 [67]. Chlorophyll-a data is available in https://doi.pangaea.de/10.1594/PANGAEA.969462. Dataset including discrete samples for total alkalinity, dissolved inorganic carbon, stable oxygen isotope composition of water, and practical salinity is available in https://doi.org/10.4211/hs.a3c0d38322fc46ea96ecea2438b29283 [68]. Air temperature data was gathered from https://doi.org/10.17897/XV96-HC57 (Greenland Ecosystem Monitoring, 2024a). Total alkalinity and pH values in Zackenberg river were gathered from https://doi.org/10.17897/1GTF-SX86 (Greenland Ecosystem Monitoring, 2024b). Precipitation data was gathered from https://doi.org/10.17897/KVVQ-BE46 (Greenland Ecosystem Monitoring, 2024c). The CTD dataset is available in https://doi.org/10.1594/PANGAEA.964983 [69]. The satellite images used in this study were provided by the Danish Meteorological Institute (https://ocean.dmi.dk/arctic/daneborg.uk.php (accessed on 16 January 2024)).

Acknowledgments: This work is a contribution to the Arctic Science Partnership (ASP). We would like to thank Egon Frandsen for logistic assistance. Generative Artificial Intelligence (ChatGPT 5.1, OpenAI) was used solely for minor linguistic improvements, such as editing grammar, spelling, and clarity of the text. The authors are fully responsible for the content and scientific interpretation of this manuscript.

Conflicts of Interest: The authors declare no conflicts of interest. The funders had no role in the design of the study; in the collection, analyses, or interpretation of data; in the writing of the manuscript; or in the decision to publish the results.

Abbreviations

The following abbreviations are used in this manuscript:

YS	Young Sound-Tyrolerfjord
CTD	Conductivity–Temperature–Depth profiler
TEOS-10	Thermodynamic Equation of Seawater (2010)
CO2SYS	Carbonate system calculation program
GEM	Greenland Ecosystem Monitoring
DMI	Danish Meteorological Institute
SA	Absolute Salinity
CT	Conservative Temperature
TA	Total Alkalinity
DIC	Dissolved Inorganic Carbon
pCO_2	Partial pressure of CO_2
pCO_2_meas	Measured pCO_2 (from CONTROS HydroC® CO_2)
pCO_2_calc	Calculated pCO_2 (from CO2SYS)
nTA, nDIC	Salinity-normalized TA and DIC
ΔDIC, ΔTA	Residuals
$DIC_{401,mix}$	DIC consistent with fixed pCO_2 = 401 under mixing assumptions

SA_{mix}, CT_{mix}, TA_{mix}, DIC_{mix}, pCO_{2mix}	Conservative-mixing expectations for SA, CT, TA, DIC, pCO_2
TA/DIC	Total Alkalinity to DIC ratio
Sref	Reference salinity
f_{fw}	Freshwater fraction
LT	Layer thickness
PP	Primary production
DIC_{pp}	DIC uptake attributable to PP
Chl-a	Chlorophyll-a
NO_3^-	Nitrate
$CaCO_3$	Calcium carbonate
$\delta^{18}O$, δ^2H	Oxygen-18 and Deuterium isotope composition
VSMOW2	Vienna Standard Mean Ocean Water 2
SLAP2	Standard Light Antarctic Precipitation 2
AMWL	Arctic Meteoric Water Line
GMWL	Global Meteoric Water Line
LRMWL	Lena River Meteoric Water Line

References

1. Perovich, D.K.; Meier, W.; Tschudi, M.; Farrell, S.; Hendricks, S.; Gerland, S.; Kaleschke, L.; Ricker, R.; Tian-Kunze, X.; Webster, M.; et al. *Sea Ice. Arctic Report Card 2019*; Richter-Menge, J., Druckenmiller, M.L., Jeffries, M., Eds.; NOAA Communications: Silver Spring, MD, USA, 2019.
2. Stroeve, J.; Notz, D. Changing State of Arctic Sea Ice across All Seasons. *Environ. Res. Lett.* **2018**, *13*, 103001. [CrossRef]
3. Bocquet, M.; Fleury, S.; Rémy, F.; Piras, F. Arctic and Antarctic Sea Ice Thickness and Volume Changes from Observations Between 1994 and 2023. *J. Geophys. Res Ocean.* **2024**, *129*, e2023JC020848. [CrossRef]
4. Renner, A.H.H.; Gerland, S.; Haas, C.; Spreen, G.; Beckers, J.F.; Hansen, E.; Nicolaus, M.; Goodwin, H. Evidence of Arctic Sea Ice Thinning from Direct Observations. *Geophys. Res. Lett.* **2014**, *41*, 5029–5036. [CrossRef]
5. Serreze, M.C.; Holland, M.M.; Stroeve, J. Perspectives on the Arctic's Shrinking Sea-Ice Cover. *Science* **2007**, *315*, 1533–1536. [CrossRef]
6. Kwok, R.; Rothrock, D.A. Decline in Arctic Sea Ice Thickness from Submarine and ICESat Records: 1958–2008. *Geophys. Res. Lett.* **2009**, *36*, L15501. [CrossRef]
7. Perovich, D.; Meier, W.; Tschudi, M.; Hendricks, S.; Petty, A.A.; Divine, D.; Farrell, S.; Gerland, S.; Haas, C.; Kaleschke, L.; et al. Sea Ice. Available online: https://arctic.noaa.gov/Report-Card/Report-Card-2020/ArtMID/7975/ArticleID/891/Sea-Ice (accessed on 25 December 2020).
8. Meier, W.N.; Petty, A.; Hendricks, S.; Perovich, D.; Farrell, S.; Webster, M.; Divine, D.; Gerland, S.; Kaleschke, L.; Ricker, R.; et al. *Sea Ice. Arctic Report Card 2022*; Druckenmiller, M.L., Thoman, R.L., Moon, T.A., Eds.; NOAA IR: Silver Spring, MD, USA, 2022.
9. Kwok, R. Arctic Sea Ice Thickness, Volume, and Multiyear Ice Coverage: Losses and Coupled Variability (1958–2018). *Environ. Res. Lett.* **2018**, *13*, 105005. [CrossRef]
10. Spreen, G.; Steur, L.; Divine, D.; Gerland, S.; Hansen, E.; Kwok, R. Arctic Sea Ice Volume Export Through Fram Strait From 1992 to 2014. *J. Geophys. Res. Ocean.* **2020**, *125*, e2019JC016039. [CrossRef]
11. Maslanik, J.; Stroeve, J.; Fowler, C.; Emery, W. Distribution and Trends in Arctic Sea Ice Age through Spring 2011. *Geophys. Res. Lett.* **2011**, *38*, L13502. [CrossRef]
12. Rutgers van der Loeff, M.M.; Cassar, N.; Nicolaus, M.; Rabe, B.; Stimac, I. The Influence of Sea Ice Cover on Air-Sea Gas Exchange Estimated with Radon-222 Profiles. *J. Geophys. Res. Ocean.* **2014**, *119*, 2735–2751. [CrossRef]
13. DeGrandpre, M.; Evans, W.; Timmermans, M.L.; Krishfield, R.; Williams, B.; Steele, M. Changes in the Arctic Ocean Carbon Cycle with Diminishing Ice Cover. *Geophys. Res. Lett.* **2020**, *47*, e2020GL088051. [CrossRef]
14. Nicolaus, M.; Katlein, C.; Maslanik, J.; Hendricks, S. Changes in Arctic Sea Ice Result in Increasing Light Transmittance and Absorption. *Geophys. Res. Lett.* **2012**, *39*. [CrossRef]
15. Katlein, C.; Arndt, S.; Nicolaus, M.; Perovich, D.K.; Jakuba, M.V.; Suman, S.; Elliott, S.; Whitcomb, L.L.; McFarland, C.J.; Gerdes, R.; et al. Influence of Ice Thickness and Surface Properties on Light Transmission through Arctic Sea Ice. *J. Geophys. Res. Ocean.* **2015**, *120*, 5932–5944. [CrossRef] [PubMed]
16. Arrigo, K.R.; Perovich, D.K.; Pickart, R.S.; Brown, Z.W.; Van Dijken, G.L.; Lowry, K.E.; Mills, M.M.; Palmer, M.A.; Balch, W.M.; Bahr, F.; et al. Massive Phytoplankton Blooms Under Arctic Sea Ice. *Science* **2012**, *336*, 1408. [CrossRef]

17. Heng, S.; Zhongyong, G.; Liqi, C.; Fan, Z. Distributions of Dissolved Inorganic Carbon and Total Alkalinity in the Western Arctic Ocean. *Adv. Polar. Sci.* **2011**, *22*, 246–252. [CrossRef]
18. Meire, L.; Søgaard, D.H.; Mortensen, J.; Meysman, F.J.R.; Soetaert, K.; Arendt, K.E.; Juul-Pedersen, T.; Blicher, M.E.; Rysgaard, S. Glacial Meltwater and Primary Production Are Drivers of Strong CO_2 Uptake in Fjord and Coastal Waters Adjacent to the Greenland Ice Sheet. *Biogeosciences* **2015**, *12*, 2347–2363. [CrossRef]
19. Yang, W.; Zhao, Y.; Wu, Y.; Chen, Z.; Gao, X.; Lin, H.; Ouyang, Z.; Cai, W.; Chen, L.; Qi, D. The Impact of Sea Ice Melt on the Evolution of Surface PCO_2 in a Polar Ocean Basin. *Front. Mar. Sci.* **2024**, *11*, 1307295. [CrossRef]
20. Rudels, B.; Carmack, E. Arctic Ocean Water Mass Structure and Circulation. *Oceanography* **2022**, *35*, 52–65. [CrossRef]
21. Duke, P.J.; Else, B.G.T.; Jones, S.F.; Marriot, S.; Ahmed, M.M.M.; Nandan, V.; Butterworth, B.; Gonski, S.F.; Dewey, R.; Sastri, A.; et al. Seasonal Marine Carbon System Processes in an Arctic Coastal Landfast Sea Ice Environment Observed with an Innovative Underwater Sensor Platform. *Elementa* **2021**, *9*, 00103. [CrossRef]
22. Rysgaard, S.; Glud, R.N.; Sejr, M.K.; Bendtsen, J.; Christensen, P.B. Inorganic Carbon Transport during Sea Ice Growth and Decay: A Carbon Pump in Polar Seas. *J. Geophys. Res. Ocean.* **2007**, *112*, C03016. [CrossRef]
23. Ericson, Y.; Falck, E.; Chierici, M.; Fransson, A.; Kristiansen, S.; Platt, S.M.; Hermansen, O.; Myhre, C.L. Temporal Variability in Surface Water PCO_2 in Adventfjorden (West Spitsbergen) with Emphasis on Physical and Biogeochemical Drivers. *J. Geophys. Res. Ocean.* **2018**, *123*, 4888–4905. [CrossRef]
24. Geilfus, N.-X.; Delille, B.; Tison, J.-L.; Lemes, M.; Rysgaard, S. Gas Dynamics within Landfast Sea Ice of an Arctic Fjord (NE Greenland) during the Spring–Summer Transition. *Elem. Sci. Anth.* **2023**, *11*, 00056. [CrossRef]
25. Rysgaard, S.; Glud, R.N.; Lennert, K.; Cooper, M.; Halden, N.; Leakey, R.J.G.; Hawthorne, F.C.; Barber, D. Ikaite Crystals in Melting Sea Ice–Implications for PCO_2 and PH Levels in Arctic Surface Waters. *Cryosphere* **2012**, *6*, 901–908. [CrossRef]
26. Lowry, K.E.; Pickart, R.S.; Selz, V.; Mills, M.M.; Pacini, A.; Lewis, K.M.; Joy-Warren, H.L.; Nobre, C.; van Dijken, G.L.; Grondin, P.L.; et al. Under-Ice Phytoplankton Blooms Inhibited by Spring Convective Mixing in Refreezing Leads. *J. Geophys. Res. Ocean.* **2018**, *123*, 90–109. [CrossRef]
27. Geilfus, N.X.; Galley, R.J.; Crabeck, O.; Papakyriakou, T.; Landy, J.; Tison, J.L.; Rysgaard, S. Inorganic Carbon Dynamics of Melt-Pond-Covered First-Year Sea Ice in the Canadian Arctic. *Biogeosciences* **2015**, *12*, 2047–2061. [CrossRef]
28. Polashenski, C.; Perovich, D.; Courville, Z. The Mechanisms of Sea Ice Melt Pond Formation and Evolution. *J. Geophys. Res. Ocean.* **2012**, *117*, C01001. [CrossRef]
29. Bakker, D.C.; Alin, S.R.; Aramaki, T.; Barbero, L.; Bates, N.; Gkritzalis, T.; Jones, S.D.; Kozyr, A.; Lauvset, S.K.; Macovei, V.A.; et al. *Surface Ocean CO_2 Atlas Database Version 2025 (SOCATv2025) (NCEI Accession 0304549)*; NOAA National Centers for Environmental Information: Asheville, NC, USA, 2025.
30. Gattuso, J.-P.; Alliouane, S.; Fischer, P. High-Frequency, Year-Round Time Series of the Carbonate Chemistry in a High-Arctic Fjord (Svalbard). *Earth Syst. Sci. Data* **2023**, *15*, 2809–2825. [CrossRef]
31. Rysgaard, S.; Vang, T.; Stjernholm, M.; Rasmussen, B.; Windelin, A.; Kiilsholm, S. Physical Conditions, Carbon Transport, and Climate Change Impacts in a Northeast Greenland Fjord. *Arct. Antarct. Alp. Res.* **2003**, *35*, 301–312. [CrossRef]
32. Bendtsen, J.; Gustafsson, K.E.; Rysgaard, S.; Vang, T. Physical conditions, dynamics and model simulations during the ice-free period of the Young Sound/Tyrolerfjord system. In *Carbon Cycling in Arctic Marine Ecosystems: Case Study Young Sound*; Rysgaard, S., Glud, R.N., Eds.; Meddelelser om Grønland; Bioscience: Copenhagen, Denmark, 2007; Volume 58, pp. 46–59.
33. Mernild, S.H.; Sigsgaard, C.; Rasch, M.; Hasholt, B.; Hansen, B.U.; Stjernholm, M.; Pedersen, D. Climate, river discharge and suspended sediment transport in the Zackenberg River drainage basin and Young Sound/Tyrolerfjord, Northeast Greenland. In *Carbon Cycling in Arctic Marine Ecosystems: Case Study Young Sound*; Rysgaard, S., Glud, R.N., Eds.; Meddr. Grønland; Bioscience: Copenhagen, Denmark, 2007; pp. 24–43.
34. McDougall, T.J.; Barker, P.M. *Getting Started with TEOS-10 and the Gibbs Seawater (GSW) Oceanographic Toolbox*; SCOR/IAPSO: Paris, France, 2011; 28p.
35. Fietzek, P.; Fiedler, B.; Steinhoff, T.; Körtzinger, A. In Situ Quality Assessment of a Novel Underwater PCO_2 Sensor Based on Membrane Equilibration and NDIR Spectrometry. *J. Atmos. Ocean. Technol.* **2014**, *31*, 181–196. [CrossRef]
36. Bauch, D.; Schlosser, P.; Fairbanks, R.G. Fresh-Water Balance and the Sources of Deep and Bottom Waters in the Arctic-Ocean Inferred from the Distribution of (H20)-O-18. *Prog. Oceanogr.* **1995**, *35*, 53–80. [CrossRef]
37. Bauch, D.; Hölemann, J.; Andersen, N.; Dobrotina, E.; Nikulina, A.; Kassens, H. The Arctic Shelf Regions as a Source of Freshwater and Brine-Enriched Waters as Revealed from Stable Oxygen Isotopes. *Polarforschung* **2010**, *80*, 127–140.
38. Ekwurzel, B.; Schlosser, P.; Mortlock, R.A.; Fairbanks, R.G.; Swift, J.H. River Runoff, Sea Ice Meltwater, and Pacific Water Distribution and Mean Residence Times in the Arctic Ocean. *J. Geophys. Res. Ocean.* **2001**, *106*, 9075–9092. [CrossRef]
39. Laukert, G.; Bauch, D.; Rabe, B.; Krumpen, T.; Damm, E.; Kienast, M.; Hathorne, E.; Vredenborg, M.; Tippenhauer, S.; Andersen, N.; et al. Dynamic Ice–Ocean Pathways along the Transpolar Drift Amplify the Dispersal of Siberian Matter. *Nat. Commun.* **2025**, *16*, 3172. [CrossRef]
40. Bowen, G.J.; Wilkinson, B. Spatial Distribution of Δ18O in Meteoric Precipitation. *Geology* **2002**, *30*, 315. [CrossRef]

41. Yi, Y.; Gibson, J.J.; Cooper, L.W.; Hélie, J.F.; Birks, S.J.; McClelland, J.W.; Holmes, R.M.; Peterson, B.J. Isotopic Signals (18O, 2H, 3H) of Six Major Rivers Draining the Pan-Arctic Watershed. *Glob. Biogeochem. Cycles* **2012**, *26*, GB1027. [CrossRef]
42. Craig, H. Isotopic Variations in Meteoric Waters. *Science* **1961**, *133*, 1702–1703. [CrossRef] [PubMed]
43. Grasshoff, K.; Kremling, K.; Ehrhardt, M. *Methods of Seawater Analysis*, 3rd ed.; John Wiley & Sons: Hoboken, NJ, USA, 2007; ISBN 9783527613984.
44. Redfield, A.C. *The Biological Control of Chemical Factors in the Environment*; Sigma Xi, The Scientific Research Honor Society: Durham, NC, USA, 1958; Volume 46, pp. 205–221.
45. Gran, G. Determination of the Equivalence Point in Potentiometric Titrations. Part II. *Analyst* **1952**, *77*, 661. [CrossRef]
46. Pierrot, D.; Lewis, E.; Wallace, D.W.R. *MS Excel Program Developed for CO_2 System Calculations. CO2Sys_v2.1.Xls*; Oak Ridge National Laboratory: Oak Ridge, TN, USA, 2006.
47. Mehrbach, C.; Culberson, C.H.; Hawley, J.E.; Pytkowicx, R.M. Measurement of the Apparent Dissociation Constants of Carbonic Acid in Seawater at Atmospheric Pressure. *Limnol. Ocean.* **1973**, *18*, 897–907. [CrossRef]
48. Dickson, A.G.; Millero, F.J. A Comparison of the Equilibrium Constants for the Dissociation of Carbonic Acid in Seawater Media. *Deep. Sea Res. Part A. Oceanogr. Res. Pap.* **1987**, *34*, 1733–1743. [CrossRef]
49. Chen, B.; Cai, W.J.; Chen, L. The Marine Carbonate System of the Arctic Ocean: Assessment of Internal Consistency and Sampling Considerations, Summer 2010. *Mar. Chem.* **2015**, *176*, 174–188. [CrossRef]
50. Woosley, R.J.; Millero, F.J.; Takahashi, T. Internal Consistency of the Inorganic Carbon System in the Arctic Ocean. *Limnol. Ocean. Methods* **2017**, *15*, 887–896. [CrossRef]
51. Rysgaard, S.; Gissel Nielsen, T.; Winding Hansen, B. Seasonal Variation in Nutrients, Pelagic Primary Production and Grazing in a High-Arctic Coastal Marine Ecosystem, Young Sound, Northeast Greenland. *Mar. Ecol. Prog. Ser.* **1999**, *179*, 13–25. [CrossRef]
52. Toole, J.M.; Timmermans, M.L.; Perovich, D.K.; Krishfield, R.A.; Proshutinsky, A.; Richter-Menge, J.A. Influences of the Ocean Surface Mixed Layer and Thermohaline Stratification on Arctic Sea Ice in the Central Canada Basin. *J. Geophys. Res. Ocean.* **2010**, *115*, C10018. [CrossRef]
53. Jackson, J.M.; Williams, W.J.; Carmack, E.C. Winter Sea-Ice Melt in the Canada Basin, Arctic Ocean. *Geophys. Res. Lett.* **2012**, *39*, L03603. [CrossRef]
54. Meyer, A.; Fer, I.; Sundfjord, A.; Peterson, A.K. Mixing Rates and Vertical Heat Fluxes North of Svalbard from Arctic Winter to Spring. *J. Geophys. Res. Ocean.* **2017**, *122*, 4569–4586. [CrossRef]
55. Koenig, Z.; Koläs, E.H.; Fer, I. Structure and Drivers of Ocean Mixing North of Svalbard in Summer and Fall 2018. *Ocean. Sci.* **2021**, *17*, 365–381. [CrossRef]
56. Friis, K.; Körtzinger, A.; Wallace, D.W.R. The Salinity Normalization of Marine Inorganic Carbon Chemistry Data. *Geophys. Res. Lett.* **2003**, *30*. [CrossRef]
57. Golden, K.M.; Eicken, H.; Heaton, A.L.; Miner, J.; Pringle, D.J.; Zhu, J. Thermal Evolution of Permeability and Microstructure in Sea Ice. *Geophys. Res. Lett.* **2007**, *34*, L16501. [CrossRef]
58. Zhou, J.; Delille, B.; Eicken, H.; Vancoppenolle, M.; Brabant, F.; Carnat, G.; Geilfus, N.; Papakyriakou, T.; Heinesch, B.; Tison, J. Physical and Biogeochemical Properties in Landfast Sea Ice (Barrow, Alaska): Insights on Brine and Gas Dynamics across Seasons. *J. Geophys. Res. Ocean.* **2013**, *118*, 3172–3189. [CrossRef]
59. Yoshimura, M.; Nomura, D.; Webb, A.L.; Li, Y.; Dall'osto, M.; Schmidt, K.; Droste, E.S.; Chamberlain, E.J.; Posman, K.M.; Angot, H.; et al. Melt Pond CO_2 Dynamics and Fluxes with the Atmosphere in the Central Arctic Ocean during the Summer-to-Autumn Transition. *Elem. Sci. Anth.* **2025**, *13*, 00023. [CrossRef]
60. Perovich, D.K.; Grenfell, T.C.; Light, B.; Hobbs, P.V. Seasonal Evolution of the Albedo of Multiyear Arctic Sea Ice. *J. Geophys. Res.* **2002**, *107*, 8044. [CrossRef]
61. Ardyna, M.; Mundy, C.J.; Mayot, N.; Matthes, L.C.; Oziel, L.; Horvat, C.; Leu, E.; Assmy, P.; Hill, V.; Matrai, P.A.; et al. Under-Ice Phytoplankton Blooms: Shedding Light on the "Invisible" Part of Arctic Primary Production. *Front. Mar. Sci.* **2020**, *7*, 608032. [CrossRef]
62. Arrigo, K.R.; Perovich, D.K.; Pickart, R.S.; Brown, Z.W.; van Dijken, G.L.; Lowry, K.E.; Mills, M.M.; Palmer, M.A.; Balch, W.M.; Bates, N.R.; et al. Phytoplankton Blooms beneath the Sea Ice in the Chukchi Sea. *Deep Sea Res. 2 Top. Stud. Ocean.* **2014**, *105*, 1–16. [CrossRef]
63. Meire, L.; Paulsen, M.L.; Meire, P.; Rysgaard, S.; Hopwood, M.J.; Sejr, M.K.; Stuart-Lee, A.; Sabbe, K.; Stock, W.; Mortensen, J. Glacier Retreat Alters Downstream Fjord Ecosystem Structure and Function in Greenland. *Nat. Geosci.* **2023**, *16*, 671–674. [CrossRef]
64. Krisch, S.; Browning, T.J.; Graeve, M.; Ludwichowski, K.U.; Lodeiro, P.; Hopwood, M.J.; Roig, S.; Yong, J.C.; Kanzow, T.; Achterberg, E.P. The Influence of Arctic Fe and Atlantic Fixed N on Summertime Primary Production in Fram Strait, North Greenland Sea. *Sci. Rep.* **2020**, *10*, 15230. [CrossRef] [PubMed]

65. Tuerena, R.E.; Hopkins, J.; Buchanan, P.J.; Ganeshram, R.S.; Norman, L.; von Appen, W.J.; Tagliabue, A.; Doncila, A.; Graeve, M.; Ludwichowski, K.U.; et al. An Arctic Strait of Two Halves: The Changing Dynamics of Nutrient Uptake and Limitation Across the Fram Strait. *Glob. Biogeochem. Cycles* **2021**, *35*, 15230. [CrossRef]
66. Assur, A. *Composition of Sea Ice and Its Tensile Strength*; Engineer Research and Development Center: Vicksburg, MS, USA, 1960.
67. Verdugo, J.; Ruiz-Castillo, E.; Rysgaard, S.; Wieter, B.; Papakyriakou, T.; Geilfus, N.-X.; Sørensen, L.L. Continuous Measurements of PCO_2 in Under-Ice Seawater during the Onset of Sea Ice Melt in Young Sound, Northeast Greenland, in 2014 [Dataset]. *Panagea* **2025**. [CrossRef]
68. Geilfus, N.-X. Young Sound 2014 [Dataset]. *HydroShare* **2022**. [CrossRef]
69. Rysgaard, S.; Boone, W.; Kirillov, S.A.; Dmitrenko, I.; Ruiz-Castillo, E. CTD Data Collected in the Period April-June 2014 in Young Sound, Greenland. *Pangaea* **2024**. [CrossRef]